Field-induced time modulation and bunching effects in photodetachment microscopy

B. C. Yang [1,*] and M. L. Du [2,†]

[1]*School of Physics and Information Technology, Shaanxi Normal University, Xi'an 710119, China*
[2]*Institute of Theoretical Physics, Chinese Academy of Sciences, Beijing 100190, China*

We present a theoretical study of the image manipulation induced by an additional oscillating electric field in traditional photodetachment microscopy. We find that the spatial electron interference image on the detecting screen perpendicular to the field is now time modulated and it varies with the oscillating field periodically. With the oscillating-field strength comparable to the static-field strength, we identify an electron bunching effect in the time domain where the electrons detached in a large time window reach the detector in a very narrow time window due to the underlying dynamics, resulting in a high concentration of detached electrons near certain observation time windows. The spatial interference images for any observational time in the narrow window show a high-intensity ring or center depending on the different electron sources. Furthermore, when the period of the oscillating field is much smaller than the flight time of the detached electrons from the negative ions to the detector, the oscillating field has a strong effect on the center of the images. On the other hand, when the oscillating-field period is comparable to or larger than the flight time of the detached electrons, the edge and the size of the interference images on the screen can be greatly modified. The accumulated electron images over time are also studied and explained using Bessel functions and stationary phase approximations.

I. INTRODUCTION

Photodetachment microscopy (PDM) has been established as a sophisticated way to image the photoelectron wave on a macroscopic scale [1–3]. In traditional PDM, the electron wave is guided by a uniform electric field to a plane detector at about a half meter away from the photodetachment source region. Following the semiclassical picture [4], the electron can generally reach each point on the detector along two different classical trajectories. As a result of quantum interferences between the electron waves associated with these two orbits, an electron image similar to Newton's rings in optics can be observed [4–7]. The number of rings and also the interference details depend on the initial kinetic energy of the electron after detached from the atomic negative ion and therefore are directly connected to the electron affinity of the specific atom. Benefiting from this energy dependence, traditional PDM provides a highly accurate measurement for electron affinities of atoms [8–13]. The quantum nature is its inherent advantage over classical electron spectrometry.

The principle of quantum interferences in PDM is general and it has been extensively studied in many other similar situations. For instance, the electron dynamics and interferences have been explored in different external fields such as parallel electric and magnetic fields [14–16], the magnetic field [17], or a repulsive field [18]. In particular, Chaibi *et al.* observed a global displacement of the photoelectron image when placing PDM in a transverse magnetic field [19,20]. This kind of interesting observation was confirmed and extended in recent theoretical work [21,22]. Furthermore, great successes have also been achieved in parallel studies based on photoionization microscopy of neutral atoms [23–32], which enables the macroscopic imaging of the atomic wave function and related stark states.

We have generalized the physical idea of PDM to temporal interferometry [33], partly inspired by the peculiar features of terahertz single-cycle pulses [34–38]. The main difference from traditional PDM is that the applied external field is time dependent instead of static. At each final time recorded on the detector, there would be two or more electron trajectories reaching the same point simultaneously. The time-dependent electron waves associated with those trajectories can also interfere quantum mechanically, showing an oscillatory electron flux in the real-time domain. Following this line of study, Ambalampitiya and Fabrikant explored the temporal interferences in a sinusoidal oscillating field based on the time-dependent Green's function [39]. By replacing the weak laser pulse with a double pulse for launching electron, Khan *et al.* examined the variation of temporal interferences with the relative delay and phases between the two pulses [40].

In comparison with traditional PDM [1,4–7], there are two obvious features among the previous studies of temporal interferences [33,39,40]. First, laser pulses with finite duration were used to replace the usual cw laser for launching electrons; otherwise the accumulated background electron may destroy the temporal interferences. Second, without using a static field to guide the general direction of electron motion, only a fraction of the outgoing electron wave was collected on the detector, which may require more experimental effort to achieve a high-quality image. Therefore, owing to some

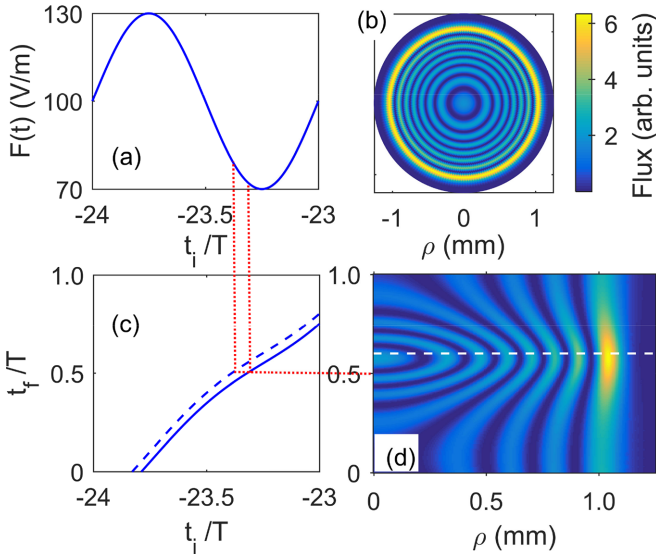*bcyang@snnu.edu.cn
†duml@itp.ac.cn

FIG. 1. Demonstration of the underlying physics induced by an oscillating electric field. (a) Total field profile, including a static electric field $F_0 = 100$ V/m and an oscillating field $F_1 \sin(\omega t)$ with $F_1 = 30$ V/m and $\omega/2\pi = 100$ MHz. (b) Electron image at $t_f = 0.6T$, with $T = 2\pi/\omega$. This cylindrical image is calculated for a detector placed perpendicular to the electric field and at $z = -0.5$ m away from the electron source. The initial energy of the electron is 0.06 meV, approximately the same as in traditional PDM [1,7]. (c) Example of the arrival-time plot connecting t_i when the electron is detached and t_f when it arrives at the center point ($\rho = 0$) on the detector. For each position ρ on the detector, there is a corresponding arrival-time plot. (d) Electron image modulated with time (vertical axis) in one period T of the oscillating field. The white dashed line cutting along the ρ direction corresponds to the image shown in (b) at that time instant. The dotted lines crossing plots (a), (c), and (d) illustrate the two trajectories reaching $\rho = 0$ at $t_f = 0.5T$ simultaneously, resulting in the temporal interferences between the two corresponding electron waves. The images shown here correspond to an s-wave source after Eq. (29), where the relative intensity of the electron flux at each point is suggested by the color bar on the right in (b). The bright spot in (d) and the bright ring in (b) are hints of an electron bunching effect in the time domain.

required technical changes with other possible challenges, we may have to wait a while to witness the experimental realization of those predictions for temporal interferences [33,39,40].

In this work we investigate how the photoelectron image could be modulated in traditional PDM when a weak oscillating electric field is applied. In the present model, both the cw laser and the static electric field in traditional PDM are kept unchanged [1,4–7], which avoids those concerns discussed above regarding the technical difficulties in an experiment, and a high-quality image would be expected. By adding an oscillating field, the static image in traditional PDM will be modulated and vary with time periodically. As demonstrated in Fig. 1, the quantum interferences occur between electron waves initially generated at different time instants but finally arriving at the detector simultaneously. Different from previous studies of temporal interferences [33,39,40], the quantum interferences at each

temporal-spatial point are only connected with two trajectories when the static electric field dominates over the added oscillating field. In other words, the original simple picture based on two trajectories for each detecting point in traditional PDM is still preserved but generalized into a time-dependent version.

Beyond the technical advantages mentioned above, the present model promises diverse phenomena and physics. When the oscillating field is weak enough or the field period is much smaller than the time of flight for the electron reaching the detector, the electron impact position on the detector is almost the same as in traditional PDM, but the interference structure is expected to vary with time clearly, caused by the variation of the accumulated phases along different trajectories. When the oscillating field is sufficiently strong with a relatively large period, the electron impact position would be changed obviously and the photoelectron rainbow structure is therefore breathing periodically with a large-range variation of the temporal image edge. Furthermore, a phenomenon which we call an electron bunching effect is found when the oscillating-field strength is comparable to the static-field value. When it takes place, many electrons detached from different instants reach the detector in a very narrow window of time due to the underlying dynamics in the combined static and oscillating electric fields. The detached electrons are therefore highly concentrated near a certain observation time, indicated by the bright spot near $t_f = 0.6T$ in Fig. 1(d). The corresponding image on the detector at that time instant is an extremely bright ring as in Fig. 1(b), where an s-wave source is considered for demonstration.

The periodicity of modulation also makes the present system distinctive and different from our previous work in Ref. [33]. The temporal-interference ripples in the previous work can be magnified in the time domain, for example, from picoseconds to microseconds in Ref. [33], analogous to the amplification of spatial-interference rings in traditional PDM. However, in the present work the temporal interferences keep varying with time periodically, though they are not magnified in the time domain. This allows us to examine an averaged temporal effect in the amplified spatial interferences after a long-time accumulation. We find that some typical features are still left in the accumulated image over time, and a good physical understanding is also achieved quantitatively.

The remainder of this paper is organized as follows. The theoretical model is specified in Sec. II, as well as some necessary formulas for semiclassical propagation. The temporal and spatial interferences are investigated in Sec. III, including the electron bunching effect in the time domain. In Sec. IV we explore the averaged image over one period, corresponding to a long-time accumulation of electron images in an experiment. A summary and brief discussion are given in Sec. V. Atomic units are used throughout this work unless specified otherwise.

II. THEORETICAL MODEL AND SEMICLASSICAL PROPAGATION

The system considered here is exactly the same as in traditional PDM [1,4,7] except for a periodically oscillating field added. The external fields $F(t)$ now include a static electric

field F_0 and an oscillating field $F_1 \sin(\omega t)$,

$$F(t) = F_0 + F_1 \sin(\omega t), \tag{1}$$

where t and ω denote the time and the field frequency, respectively. The corresponding vector potential $A(t)$ is

$$A(t) = -F_0 t + \frac{F_1}{\omega} \cos(\omega t). \tag{2}$$

Both fields are in the positive-z direction. The total field strength $F_m = F_0 + F_1$ is assumed not strong enough to obviously affect the photoabsorption process for generating an initially outgoing electron wave. The oscillating field, such as a microwave or terahertz field, varies much slower than the laser field for detaching electrons.

In the photodetachment source region, we have the interaction between an atomic negative ion and a weak cw laser linearly polarized along the z axis. The loosely bound electron is detached by absorbing one photon from the laser, which generates an outgoing electron wave

$$\psi_0(R, \theta_i, \phi_i, t_i) = \psi_{\text{out}}(R, \theta_i, \phi_i) e^{-iE_0 t_i} \tag{3}$$

at the initial time instant t_i with an energy $E_0 = k_0^2/2$. The spherical coordinates R, θ_i, and ϕ_i represent the electron position relative to the source point, which was selected as the coordinate origin. The time-independent part $\psi_{\text{out}}(R, \theta_i, \phi_i)$ is a spherically outgoing wave

$$\psi_{\text{out}}(R, \theta_i, \phi_i) = C(k_0) Y_{lm}(\theta_i, \phi_i) \frac{e^{ik_0 R}}{R}, \tag{4}$$

when the electron goes away from the rest atom. The complex coefficient $C(k_0)$ depends on the electron energy E_0 and the spherical harmonic function $Y_{lm}(\theta_i, \phi_i)$ represents the angular distribution of the initially outgoing wave. The quantum numbers l and m are determined by specific negative ion. For instance, the photodetachment of a ground state H$^-$ anion (initially in an s state) generates an outgoing p_z wave with $l = 1$ and $m = 0$; the photodetachment of a ground state F$^-$ anion (initially in a p state) corresponds to an s wave with $l = 0$ and $m = 0$, where the d-wave component of the photoelectron is largely suppressed as a result of the Wigner threshold law [41]. Note that the applied weak laser field has been assumed to be linearly polarized along the z axis.

For the electron motion in external fields, the Hamiltonian can be written as

$$H(\rho, z, p_\rho, p_z, t) = \frac{p_z^2}{2} + \frac{p_\rho^2}{2} + F(t)z, \tag{5}$$

where ρ and z represent the electron position and p_ρ and p_z the momentum in the cylindrical coordinate frame. The classical equations for ρ, z, p_ρ, and p_z can be explicitly written as, respectively,

$$p_\rho = k_0 \sin(\theta_i), \tag{6}$$

$$p_z(t) = k_0 \cos(\theta_i) + \Delta p_z(t_i, t), \tag{7}$$

$$\rho(t) = k_0(t - t_i) \sin(\theta_i), \tag{8}$$

$$z(t) = k_0(t - t_i) \cos(\theta_i) + \Delta z(t_i, t), \tag{9}$$

with

$$\Delta p_z(t_i, t) = A(t) - A(t_i), \tag{10}$$

$$\Delta z(t_i, t) = -\frac{1}{2} F_0 \tau^2 - \frac{F_1 \tau}{\omega} \cos(\omega t_i)$$
$$+ \frac{F_1}{\omega^2} [\sin(\omega t) - \sin(\omega t_i)], \tag{11}$$

where $\tau = t - t_i$ is the electron propagation time after the electron is detached from the original negative ion. Using the above equations, all of the classical electron trajectories could be followed from the source point with different initial conditions t_i and θ_i to a certain point on the detector.

Having the information of classical trajectories, one can easily follow the electron-wave propagation in a semiclassical way. The general idea is that there is an electron wave associated with each classical trajectory. The quantum wave at a certain point is a coherent superposition of electron waves associated with all the trajectories reaching that point simultaneously,

$$\Psi(\rho, z, t) = \sum_\nu \psi_\nu(\rho, z, t), \tag{12}$$

where the subscript ν is used to label the corresponding trajectory. The semiclassical wave along each trajectory can be constructed in an augmented phase space by including the time t and its conjugate momentum $p_t = -H(t)$ as two additional dimensions [33,42]. The details can be found in our previous work [33].

The general form of ψ_ν was already obtained in Ref. [33],

$$\psi_\nu(\rho, z, t) = \psi_{\text{out}}(R, \theta_i) \mathcal{A} e^{i(\tilde{S} - \lambda\pi/2)}, \tag{13}$$

where the azimuthal angle ϕ plays no role in our work and it is therefore not explicitly written out. The semiclassical amplitude $\mathcal{A}$ has a simple expression [33]

$$\mathcal{A} = \left| \frac{R^2}{k_0(t - t_i)^2 [k_0 - F(t_i)(t - t_i) \cos(\theta_i)]} \right|^{1/2}. \tag{14}$$

The Maslov index $\lambda = 0$ if $k_0 - F(t_i)(t - t_i) \cos(\theta_i) > 0$ and $\lambda = 1$ if $k_0 - F(t_i)(t - t_i) \cos(\theta_i) < 0$. The phase $\tilde{S}$ is given by

$$\tilde{S} = S - E_0 t_i, \tag{15}$$

which contains an initial phase in Eq. (3). The classical action S follows the standard definition in the augmented phase space,

$$S = \int p_\rho d\rho + p_z dz - H(t) dt, \tag{16}$$

which has been transformed into [33]

$$S = E_0(t - t_i) + z(t) \Delta p_z(t) - \frac{1}{2} \int [\Delta p_z(t)]^2 dt. \tag{17}$$

Note that the phase given by Eq. (15) contains all the time-dependent phases. It is not directly equal to the classical action $S_0 (= \int \mathbf{p} \cdot d\mathbf{q})$ usually used in static external fields. Instead,

$$\tilde{S}_0 = S_0 - E_0 t, \tag{18}$$

where $\tilde{\mathcal{S}}_0$ represents the value of $\tilde{\mathcal{S}}$ in a static field. However, it does not affect the phase difference between trajectories reaching the detector simultaneously, namely,

$$\Delta\tilde{\mathcal{S}}_0 = \Delta S_0, \tag{19}$$

which will be used in calculating the electron image.

III. TEMPORAL IMAGE AND BUNCHING EFFECT

In the following analysis and calculations, we choose $E_0 = 0.06$ meV and $F_0 = 100$ V/m, which are approximately the parameters in traditional PDM [1,7]. A high-resolution detector is also assumed to be placed at $z_f = -0.5$ m away from the photodetachment source region and the detector surface is perpendicular to the z axis. The oscillating-field strength could be changed to examine the field-induced modulation effects when necessary. The field default frequency is 100 MHz unless specified otherwise.

In this section we focus on how the electron image would be modulated with time when the weak oscillating field is applied, as well as an electron bunching effect. To be clear, we first present a general consideration and related formulas, followed by some representative calculations and discussion.

A. General considerations and related formulas

The electron image on the detector corresponds to a generalized differential cross section $d\sigma/ds$ [4],

$$\frac{d\sigma}{ds} = \frac{2\pi E_{\text{ph}}}{c}\mathbf{j}\cdot\mathbf{n}, \tag{20}$$

where ds is the differential area on the detector surface, E_{ph} denotes the photon energy from the laser field, c is the speed of light, $\mathbf{j} = \text{Im}(\Psi^*\nabla\Psi)$ is the electron flux crossing the detector surface, and $\mathbf{n}$ is the exterior norm vector on the detector surface. For clarity and convenience in applications, a reduced flux $\tilde{j}_z$ can be defined as

$$\tilde{j}_z = -\text{Im}\left[\left(\sum_\nu\tilde{\psi}_\nu\right)^*\frac{\partial}{\partial z}\left(\sum_\nu\tilde{\psi}_\nu\right)\right], \tag{21}$$

which is obtained by combining Eqs. (4), (12), (13), and (20) and getting rid of those constant factors. The minus sign appears because the exterior norm vector $\mathbf{n}$ is along the negative-z axis in our present work. The simplified form of the wave function $\tilde{\psi}_\nu$ can be written as

$$\tilde{\psi}_\nu^s(\rho, z, t) = \tilde{A}_\nu e^{i(\tilde{\mathcal{S}}_\nu - \lambda_\nu\pi/2)} \tag{22}$$

for an s-wave source such as the photodetachment of F^-. Here $\tilde{A} = \mathcal{A}/R$. For a p_z-wave source such as the photodetachment of H^-, $\tilde{\psi}_\nu$ is simplified as

$$\tilde{\psi}_\nu^p(\rho, z, t) = \tilde{A}_\nu\cos(\theta_i)e^{i(\tilde{\mathcal{S}}_\nu - \lambda_\nu\pi/2)}. \tag{23}$$

By counting all of the electron waves associated with each classical trajectory, the electron flux can be calculated in principle after Eq. (21), corresponding to the electron image on the detector in arbitrary units.

In our present system, the weak oscillating field does not destroy the qualitative interference picture. As shown in Fig. 2, there are still two trajectories reaching each point on
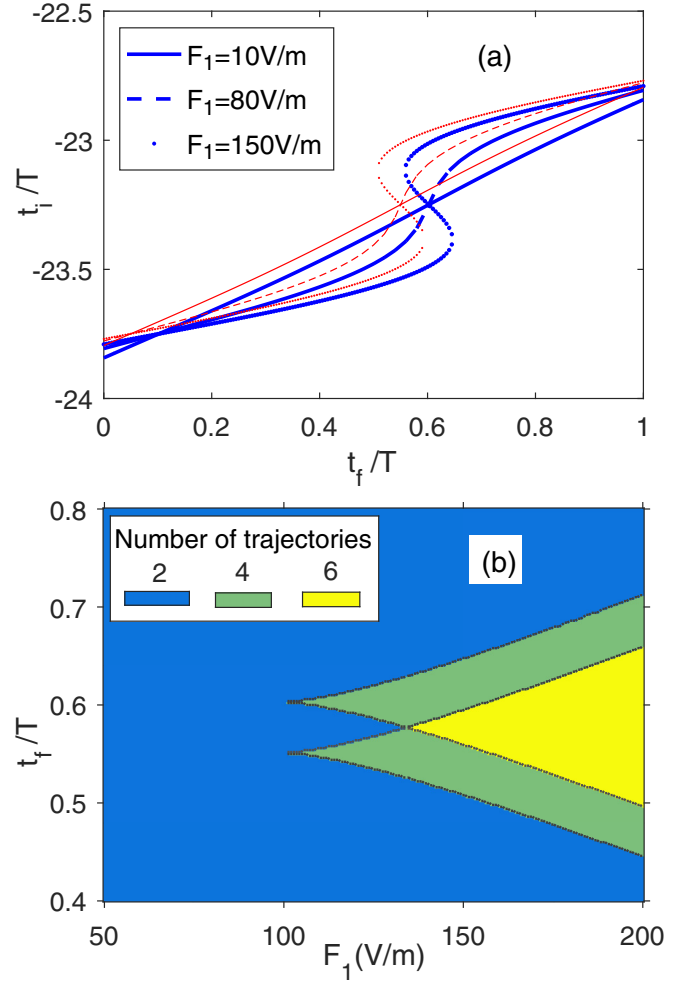

FIG. 2. (a) Arrival-time plot for the electron reaching the detector center, with different oscillating-field strengths given in the legend. The bold blue lines are those trajectories with $\theta_i = 0$ and the thin red lines are those with $\theta_i = \pi$. (b) Total number of trajectories (shown by different colors in the legend) reaching the detector center at each final time as a function of the oscillating-field strength. The dotted lines mark the locations of temporal caustics.

the detector simultaneously in the weak-field regime. For the electron image involving two trajectories at each point, we have

$$\tilde{j}_z = -p_{z_1}\tilde{A}_1^2 - p_{z_2}\tilde{A}_2^2 - (p_{z_1} + p_{z_2})\tilde{A}_1\tilde{A}_2\cos(\Delta\varpi_{12}) \tag{24}$$

for an s-wave electron source and

$$\tilde{j}_z = -p_{z_1}\tilde{A}_1^2\cos^2(\theta_{i1}) - p_{z_2}\tilde{A}_2^2\cos^2(\theta_{i2}) - (p_{z_1} + p_{z_2})$$
$$\times \tilde{A}_1\tilde{A}_2\cos(\theta_{i1})\cos(\theta_{i2})\cos(\Delta\varpi_{12}) \tag{25}$$

for a p_z-wave electron source, where

$$\Delta\varpi_{12} = \Delta\tilde{\mathcal{S}} - \pi/2, \tag{26}$$

with

$$\Delta\tilde{\mathcal{S}} = \tilde{\mathcal{S}}_1 - \tilde{\mathcal{S}}_2. \tag{27}$$

The two trajectories have been ordered in Eq. (27) such that the trajectory labeled by the subscript 1 has a Maslov index of unity, while the other trajectory has a zero value

of Maslov index. The practical calculations using Eq. (27) involve the difference between huge values of $\tilde{S}_1$ and $\tilde{S}_2$. We therefore avoid the direct calculations of $\tilde{S}_1$ or $\tilde{S}_2$, but combine the formulas in Eqs. (10), (17), and (27) to an applicable form as follows for $\Delta\tilde{S}$:

$$\Delta\tilde{S} = 2E_0(t_{i2} - t_{i1}) + z(t)[A(t_{i2}) - A(t_{i1})]$$
$$- \frac{1}{2}A^2(t_{i1})(t - t_{i1}) + \frac{1}{2}A^2(t_{i2})(t - t_{i2})$$
$$+ A(t_{i1})\int_{t_{i1}}^{t} A(t')dt' - A(t_{i2})\int_{t_{i2}}^{t} A(t')dt'$$
$$+ \frac{1}{2}\int_{t_{i2}}^{t_{i1}} A^2(t')dt'. \tag{28}$$

The two integrals involved in this equation can be readily written as

$$\int_{t_i}^{t} A(t')dt' = -\frac{F_0}{2}\left(t^2 - t_i^2\right) + \frac{F_1}{\omega^2}[\sin(\omega t) - \sin(\omega t_i)]$$

and

$$\int_{t_{i2}}^{t_{i1}} A^2(t')dt' = \frac{F_0^2}{3}\left(t_{i1}^3 - t_{i2}^3\right) + \frac{F_1^2}{2\omega^2}(t_{i1} - t_{i2})$$
$$+ \frac{F_1^2}{4\omega^3}[\sin(2\omega t_{i1}) - \sin(2\omega t_{i2})]$$
$$- \frac{2F_0 F_1}{\omega^2}[t_{i1}\sin(\omega t_{i1}) - t_{i2}\sin(\omega t_{i2})]$$
$$- \frac{2F_0 F_1}{\omega^3}[\cos(\omega t_{i1}) - \cos(\omega t_{i2})].$$

The primitive semiclassical formulas in Eqs. (24) and (25) are known to diverge at the classical boundary. They are usually repaired following some kind of uniform approximation near the classical boundary. In this spirit and similar to the manipulations in Ref. [18], the flux formula in Eq. (24) can be written as

$$\tilde{j}_z = P\,\text{Ai}^2(\zeta) + Q\,\text{Ai}'^2(\zeta), \tag{29}$$

where $\text{Ai}(\zeta)$ and $\text{Ai}'(\zeta)$ are the Airy function and its first-order derivative, respectively,

$$\zeta = -\left(\frac{3}{4}\tilde{S}\right)^{2/3}, \tag{30}$$

$$P = -\pi|\zeta|^{1/2}\big[p_{z_1}\tilde{A}_1^2 + p_{z_2}\tilde{A}_2^2 + (p_{z_1} + p_{z_2})\tilde{A}_1\tilde{A}_2\big], \tag{31}$$

$$Q = -\pi|\zeta|^{-1/2}\big[p_{z_1}\tilde{A}_1^2 + p_{z_2}\tilde{A}_2^2 - (p_{z_1} + p_{z_2})\tilde{A}_1\tilde{A}_2\big]. \tag{32}$$

The flux formula in Eq. (25) for a p_z-wave source can also be written in the same form as in Eq. (29) after replacing $\tilde{A}_\nu$ in Eqs. (31) and (32) by the combined term $\tilde{A}_\nu\cos(\theta_i)$. The modified expression in Eq. (29) now behaves correctly near the classical boundary and it could be easily extended into the classically forbidden region by following the approximately linear-variation property of those quantities in Eqs. (30)–(32).

B. Specific calculations and discussion

To calculate the electron flux based on the semiclassical scheme, all of those trajectories reaching a certain point (ρ, z) on the detector at a final time t must be identified with both

their initially outgoing angle θ_i and the initial time t_i. For generality, one can first search all the solutions of t_i after the equation

$$[z(t) - \Delta z(t_i, t)]^2 + \rho^2 = k_0^2(t - t_i)^2, \tag{33}$$

with $\Delta z(t_i, t)$ given by Eq. (11), and then calculate θ_i as

$$\theta_i = \arccos\left(\frac{z(t) - \Delta z(t_i, t)}{k_0(t - t_i)}\right). \tag{34}$$

The connections between t_f and t_i are explored in Fig. 2 by considering those trajectories reaching the detector center ($\rho = 0$) located at $z_f = -0.5$ m. The arrival-time plot in Fig. 2(a) shows some typical curves of t_i as a function of the final time t_f. The number of solutions of t_i for each t_f suggests the total number of trajectories along which the electron propagates to the same imaging point. It is given by the number of crossings between each pair of the curves having the same line style in Fig. 2(a) with a vertical line at each t_f. It is obvious that for $F_1 = 150$ V/m in Fig. 2(a) one can find six trajectories in the middle of the S-shaped curves. To get a whole picture of where the number of trajectories changes, a two-dimensional plot is given in Fig. 2(b) by increasing the oscillating-field strength continuously. The borders marked by the black dotted lines are the locations of temporal caustics, given by

$$F(t_i)(t - t_i)\cos(\theta_i) = k_0, \tag{35}$$

where the semiclassical amplitude in Eq. (14) goes to infinity and the semiclassical wave needs to be repaired using a uniform approximation.

It can be learned from Fig. 2(b) that the number of contributed trajectories starts to change at the emerging point of temporal caustics near $F_1 = F_0$. For a weak oscillating field where the field strength is less than the static-field value, we still have the two-trajectory picture as in traditional PDM. The studies where the oscillating field dominates over the static field are irrelevant in this work. Furthermore, we have not gained much useful information from our draft calculations in the strong-field regime, except for an observation of extremely rapid oscillations. Therefore, we confine ourselves to the modulation effects caused by a weak oscillating field in traditional PDM, where some interesting physics is explored.

1. Temporal-spatial modulations of electron flux

In Fig. 3 the electron flux is calculated by scanning over time at the detector center for different oscillating fields. The modulation effects are obvious, owing to the temporal interferences between electron waves associated with the two trajectories reaching the detector at each final time, as illustrated in Fig. 1. An out-of-phase oscillation can be observed between those results for s-wave and p-wave sources, which has been established as a common feature in previous studies [33]. It can be traced back to the different angular distribution of the initially outgoing wave when generated from the two different sources, by noting that the factor $\cos(\theta_{i1})\cos(\theta_{i2})$ contributes a minus sign in Eq. (25).

To get a picture of how the electron image at different positions could be modulated by an oscillating field, the temporal-spatial pattern of the whole image on the detector is displayed in Fig. 4, corresponding to the four cases in Fig. 3.
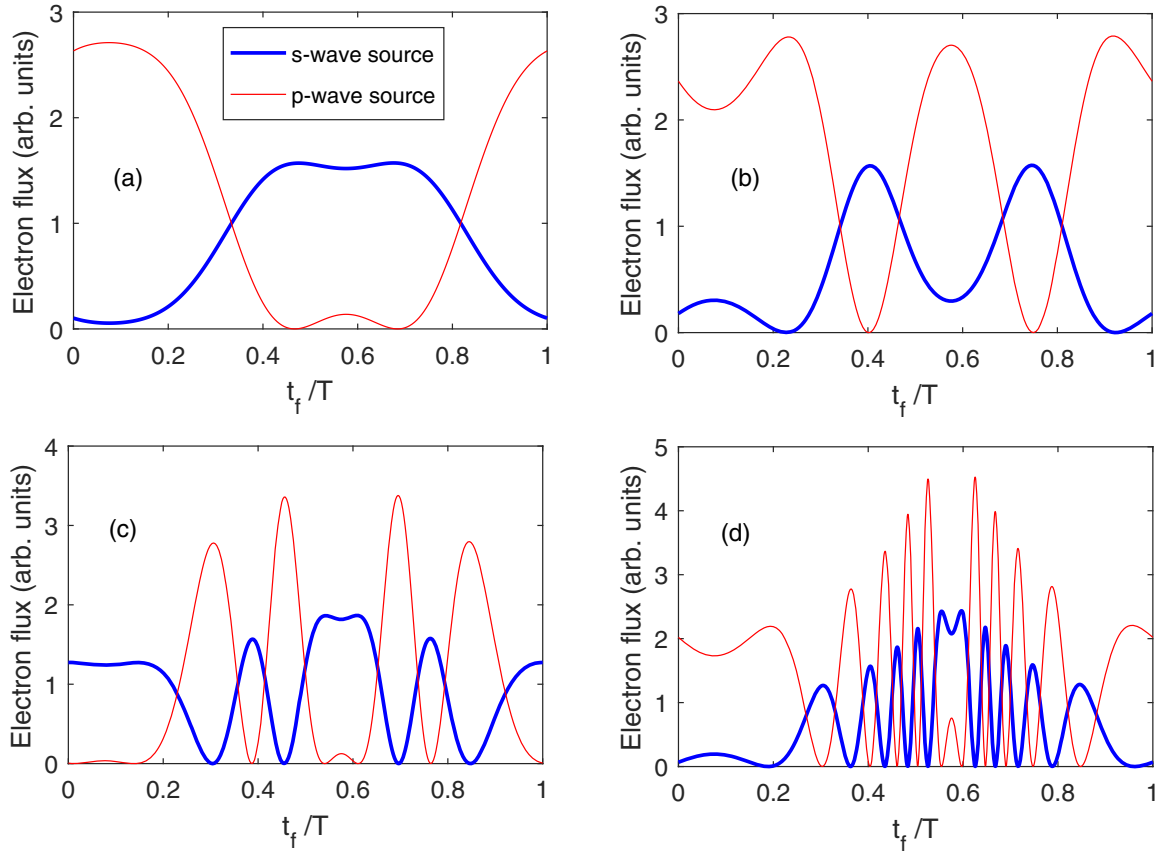
FIG. 3. Electron flux calculated at the detector center for different field strengths: (a) $F_1 = 5$ V/m, (b) $F_1 = 10$ V/m, (c) $F_1 = 20$ V/m and (d) $F_1 = 40$ V/m. The bold blue and the thin red lines display the flux modulations for s-wave and p-wave sources, respectively.

One immediate observation is that the electron image near the detector center is modulated obviously. The field-induced time modulation becomes weak gradually with the position moving away from the center point. In addition, the image near the classical boundary, namely, the outermost ring on the detector as shown in Fig. 1, shows no obvious modulation. This can be understood by examining the difference of the phase accumulation along each pair of trajectories reaching different positions.

The position dependence of $\Delta\tilde{S}$ is explored in Fig. 5 by taking $t_f = 0.6T$ as an example, because the spatial modulation near this time is quite obvious in Fig. 4. The value

of $\Delta\tilde{S}$ decreases gradually from a finite value at the center point to a zero value at the classical boundary. This behavior is general and it is closely connected with the dynamic differences between the two trajectories involved. Near the center point, both the initial time t_i and the initially outgoing angle θ_i are largely different between the two trajectories reaching the same point. These differences explain the large and finite value of $\Delta\tilde{S}_{\text{static}}$ and can be easily changed when the electron dynamics is modulated by the oscillating field. However, near the classical boundary, the differences between the two trajectories becomes small, including the initial conditions t_i and θ_i. More importantly, these differences eventually go to zero
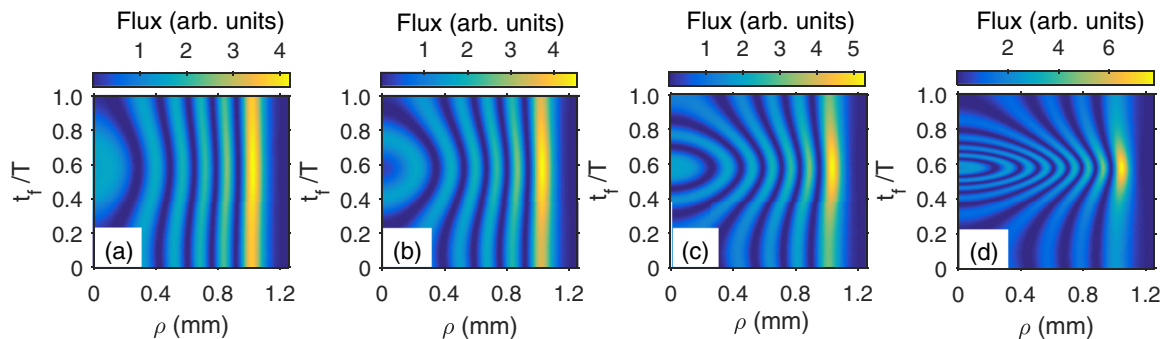

FIG. 4. Temporal-spatial pattern of the electron image on the detector. All the results shown here correspond to an s-wave electron source after Eq. (29) for (a) $F_1 = 5$ V/m, (b) $F_1 = 10$ V/m, (c) $F_1 = 20$ V/m, and (d) $F_1 = 40$ V/m. The color bar on top of each plot suggests the relative intensity of the electron flux at each point.
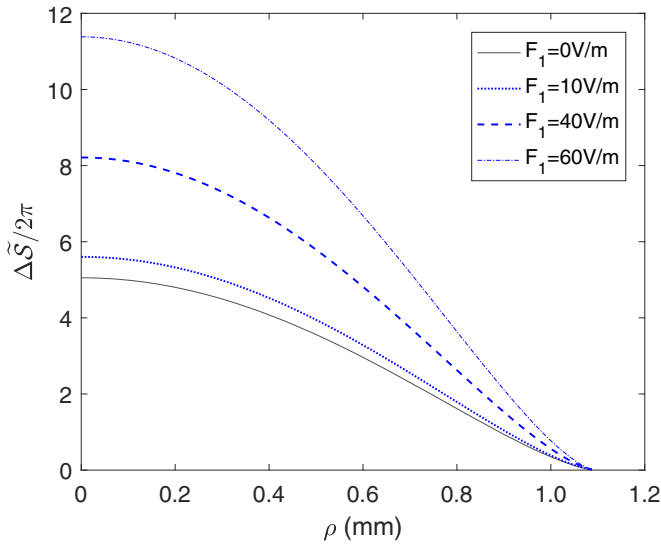
FIG. 5. Spatial variation of $\Delta\tilde{\mathcal{S}}/2\pi$ on the detector. The field values are given in the legend, where $F_1 = 0$ V/m means only the static field applies. All the calculations are performed for $t_f = 0.6T$ as in Fig. 4.

exactly when reaching the classical boundary, where the two trajectories actually coincide as one trajectory, regardless of whether the applied oscillating-field strength is zero or large. This universal behavior explains why the interference structure near the image edge is hardly changed by an oscillating field. On the other hand, the values of $\Delta\tilde{\mathcal{S}}/2\pi$ at $\rho = 0$ in Fig. 5 count the number of spatial interference rings in Fig. 4 at the corresponding final time. By looking at those images shown in Fig. 4, one may notice that the spatial location of the image edge is almost unchanged with time. This is because the period T of the added oscillating field is much smaller than the time of flight ($\tau = t_f - t_i$) for the electron reaching the detector [Fig. 1(c)]. After Eqs. (11) and (33), the electron impact position on the detector is almost the same as that in traditional PDM with only a static electric field, as long as $F_1 T/F_0 \tau \ll 1$ is satisfied. Under this condition, the classical boundary of the electron impact position on the detector is therefore stable against the added oscillating field, which corresponds to those stable locations of the image edge in Fig. 4.

The electron impact position would be different if a limiting case were considered where the added oscillating field is sufficiently strong with a larger period T compared with τ. A typical image is shown in Fig. 6 for both s-wave and p-wave sources, where $F_1 = 40$ V/m, the same value as in Fig. 4(d), but the field frequency has been changed from 100 MHz to 1 MHz. Now T is about four times τ on average. With $\omega/2\pi = 1$ MHz, the terms caused by the oscillating field in Eq. (11) are not negligibly small, and the electron impact position on the detector is therefore obviously different from that in traditional PDM according to Eq. (33). The resulting effect can be seen in the temporal variation of the classical boundary, as depicted by the white dashed curves in Figs. 6(a) and 6(b). Note that the electron image is still modulated periodically, which originates in the periodicity of the field. However, the intensity of flux imaged in the first half period is
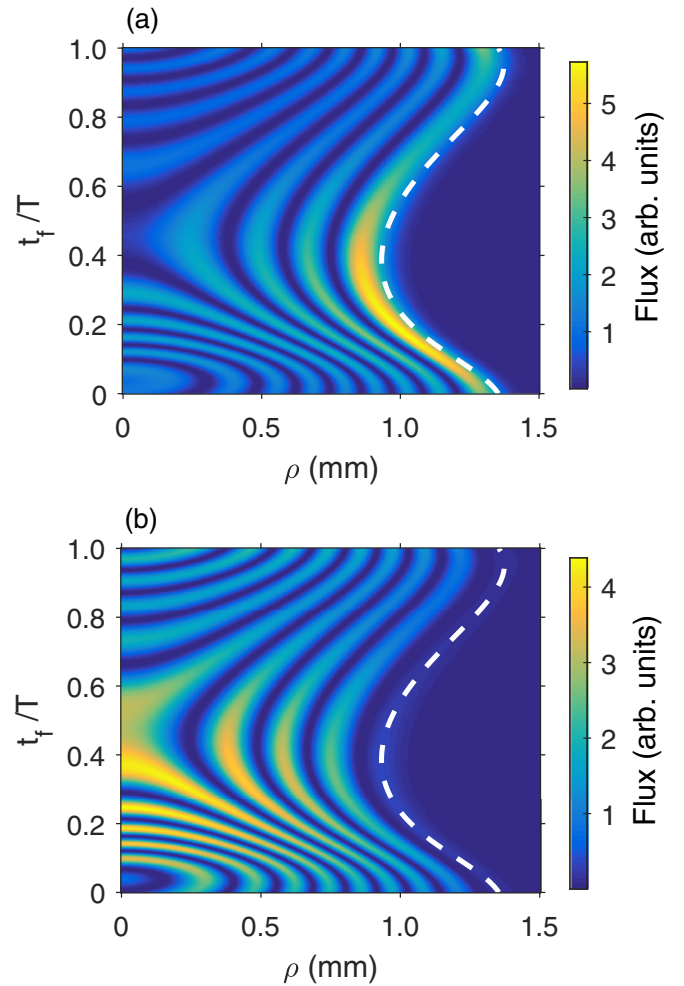

FIG. 6. Limiting case where $\omega/2\pi = 1$ MHz and $F_1 = 40$ V/m, so that the field period is longer than the time of flight for the electron reaching the detector, for the temporal-spatial pattern of the electron image from (a) s-wave and (b) p-wave sources. The relative flux intensity at each point is indicated by the color bar to the right of each plot. The white dashed curves mark those locations of the classical boundary at each time instant.

apparently higher than that recorded in the second half period. This is attributed to the relatively strong field affected by the electron when flying to the detector in the first half period [Fig. 1(a)].

2. Bunching effect and localized coherent electron pulses

Another important feature exhibited by Figs. 3 and 4 is the visual clustering of the quantum oscillations. With the oscillating-field strength increased gradually, the enriched quantum modulations tend to be localized in a narrower range of time, where an approximate symmetrical distribution is observed. As a straightforward way to understand these peculiar features, we plot in Fig. 7 the phase difference $\Delta\tilde{\mathcal{S}}/2\pi$ between the two trajectories involved in the quantum interferences, as well as the semiclassical amplitudes $\tilde{A}_i$ accumulated along the two trajectories. Based on the local values symmetrically distributed in Fig. 7, the symmetric distribution of those modulations in Figs. 3 and 4 seems to be understood.
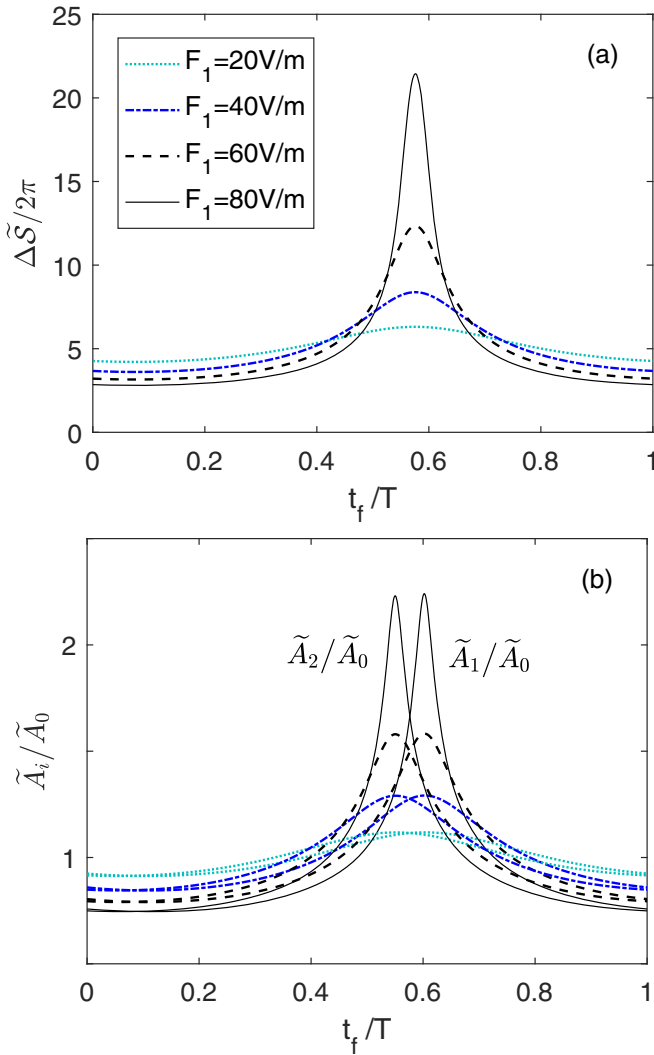
FIG. 7. (a) Temporal variation of the phase difference $\Delta\tilde{\mathcal{S}}/2\pi$ between the two trajectories reaching the detector center simultaneously. (b) Temporal variation of the semiclassical amplitude $\tilde{A}_i$ accumulated along each trajectory, divided by the corresponding amplitude $\tilde{A}_0$ in the static field only. The results for different field strengths are shown in both (a) and (b), as specified in the legend. The group of lines on the right-hand side in (b) are those amplitudes accumulated along the trajectory from $\theta_i = 0$ and the other group on the left-hand side corresponds to the trajectory from $\theta_i = \pi$.

The actual question now is what kind of dynamics makes those local distributions. The rapidly increasing behavior of the semiclassical amplitude in Fig. 7(b) gives us a hint to find the answer. Note that the accumulated amplitude actually suggests the relative density of the electron at different places when moving along classical trajectories [18]. The locally large amplitude tells us that the electrons are concentrated around that local time range. Keeping this in mind, the shape variation of the arrival-time plot in Fig. 2 draws our attention.

It turns out that the visual clustering of those rich oscillations in Figs. 3 and 4 can be graphically explained based on the arrival-time plot in Fig. 2. When the oscillating-field strength is close to a critical point of temporal caustics near 100 V/m in Fig. 2(b), the two curves for each pair of

trajectories in Fig. 2(a) bend up locally in the vertical direction in the arrival-time plot. The direct consequence of this vertical curve bending is that the electron from a large range of initial detaching time will reach the detector in a very narrow range of final time, inducing an electron bunching dynamics in the time domain, and large values of the accumulated amplitudes are expected. Meanwhile, in the process of curve bending, the two curves separate from each other as shown in Fig. 2(a), and the difference between t_i becomes large. The phase difference $\Delta\tilde{\mathcal{S}}$ between the two trajectories is therefore largely increased, resulting in rapid oscillations with large amplitudes.

Based on the above physical picture, the electron bunching effect should be more obvious when the oscillating-field strength gets closer to the critical point of temporal caustics. As shown in Fig. 8, almost all of the temporal oscillations are bunched together within a small part of one period. In particular, for an s-wave source, since the quantum interferences are limited near the classical boundary, a bright spot appears in Fig. 8(b), which means that in an experiment one may record a bright electron ring on the detector periodically. For a p-wave source as in Fig. 8(c), the interference rings are folded into a small time window, and a periodically breathing of the bright rings would be observed in a similar experiment.

The interplay between the electron bunching effect and quantum interferences produces a train of periodic intense electron pulses impacting on the detector, and these electron pulses have their own temporal-spatial interference structure. To be clear, a series of the visual images expected near the bunching regime is shown in Fig. 8(d) which assumes a temporal resolution of 1 ns in a real experiment. Each visual image recorded at the time t_f in Fig. 8(d) is an average of those corresponding images from Figs. 8(b) and 8(c) in the time interval between $t_f - 0.5$ and $t_f + 0.5$ ns. The coherent electron pulses can be clearly observed as those localized bright rings on the detector, flashing periodically like that recorded at $t_f = 0.6T$ in Fig. 8(d). Within a feasible range of experimental resolution, one can properly increase the oscillating-field strength to make the bunching effect stronger so that the localized electron-flux intensity becomes larger, which would make it much easier to achieve a high-quality image.

The bunching effect as shown in Fig. 8 cannot be achieved with a single oscillating electric field (without a static field). By examining the arrival-time plots for the photoelectron in a single oscillating field, we find that a similar curve bending may exist for some special trajectories (such as $\theta_i = 0$ and π) when F_1 is around 250 μV/m, which can be estimated from Eq. (35). However, with such an extremely weak oscillating field only, the trajectories cannot even reach the detector on the same side and the electron current is extremely weak with no quantum interference. Therefore, the combination of the static and the oscillating electric fields is essential for observing the phenomena discussed above.

IV. ACCUMULATED IMAGE OVER TIME

Since the spatial image is modulated with time, it is natural to ask what kind of features could be left after a long-time accumulation. For this purpose, an averaged image over one
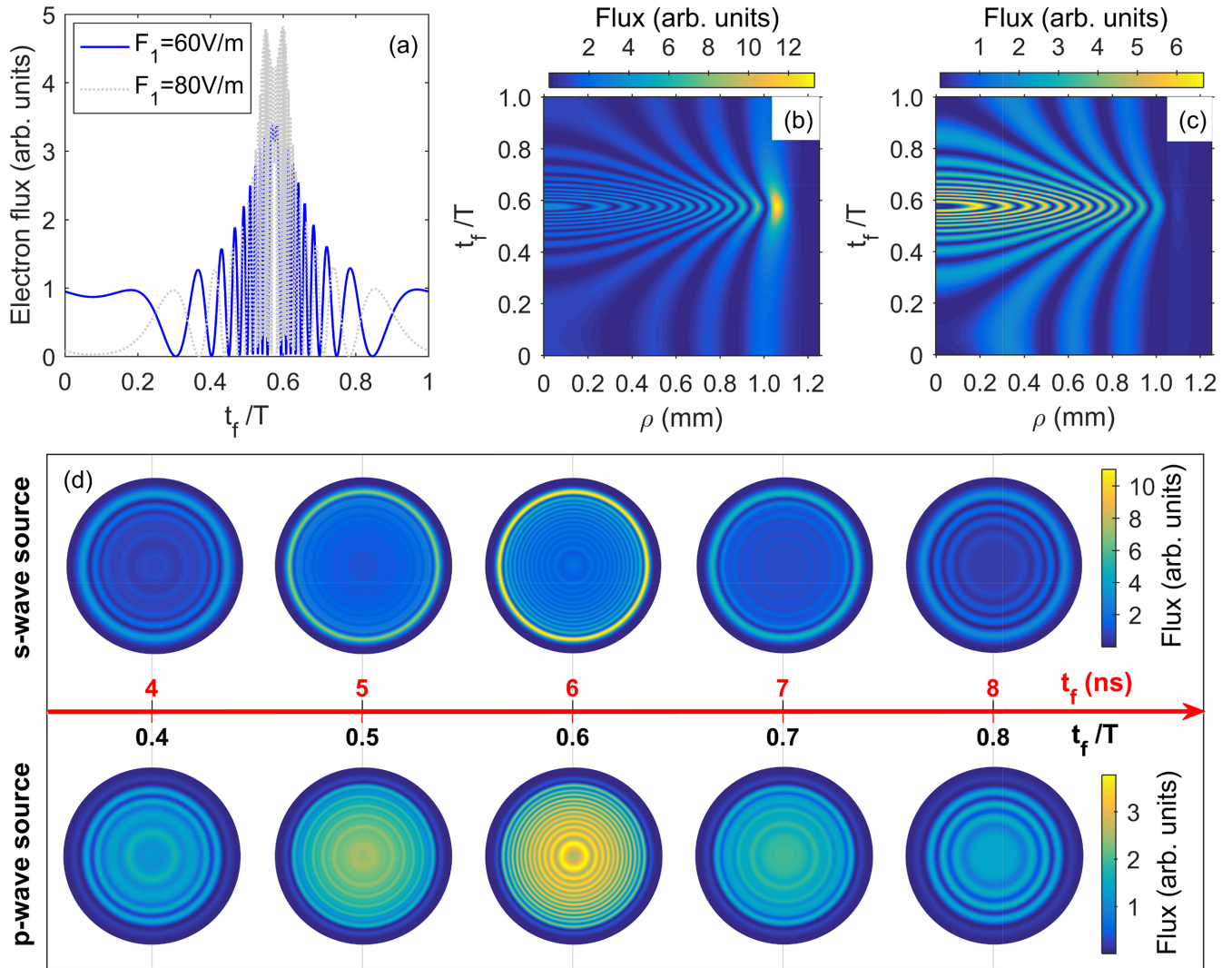
FIG. 8. Electron bunching effect when the oscillating-field strength F_1 is comparable to the static-field strength. (a) Temporal electron flux calculated at the detector center for an s-wave source after Eq. (29). The temporal-spatial pattern of the electron image when $F_1 = 60$ V/m is shown for (b) s-wave and (c) p-wave sources. The color bar on top of each plot suggests the relative intensity of the electron flux at each point. (d) Visual images expected at each time instant with a temporal resolution of 1 ns. The time axis is in units of both nanoseconds and T for a comparative understanding. The images above and below the time axis correspond to the finite-resolution slices from (b) and (c), respectively, with the relative flux intensity at each point suggested by the color bar to the right of each row.

period can be defined as

$$\overline{J_z} = \frac{1}{T} \int_0^T \tilde{j}_z \, dt, \tag{36}$$

corresponding to an experimental accumulation on a detector for many cycles of the oscillating field. Although some kind of temporal features would generally be expected to be weakened after an operation of averaging, we find that several peculiar phenomena can still be observed in the accumulated image over time. To study this kind of accumulated effect, we choose to first integrate the temporal image directly over one period and then find a quantitative understanding based on a perturbation theory and the stationary phase approximation, respectively. A simple semiclassical picture is finally established for those rest interferences observed in the accumulated electron image over time.

The integrated electron image on the detector center is first examined in Fig. 9 as a function of the oscillating-field strength. The thin solid curves are given by the direct integration after Eq. (36). Both curves have been divided by the electron image with only a static field. Accordingly, both curves start from one on the y axis in Fig. 9, as they should. It can be observed that the flux intensity in the averaged image is still modulated obviously by the oscillating field. The averaged spatial images from the direct integration are also shown in Figs. 10–13. Some interesting features can be observed in Figs. 10–13, such as the amplitude weakening effect in Fig. 10 and the rest oscillations in Figs. 11–13. To reveal the physics behind the data, further analysis is presented in the following sections with the guidance of intuitive insight. Although the direct integration cannot provide a satisfactory explanation, it is thought to be accurate and will be used as a reliable data reference in the following analysis.
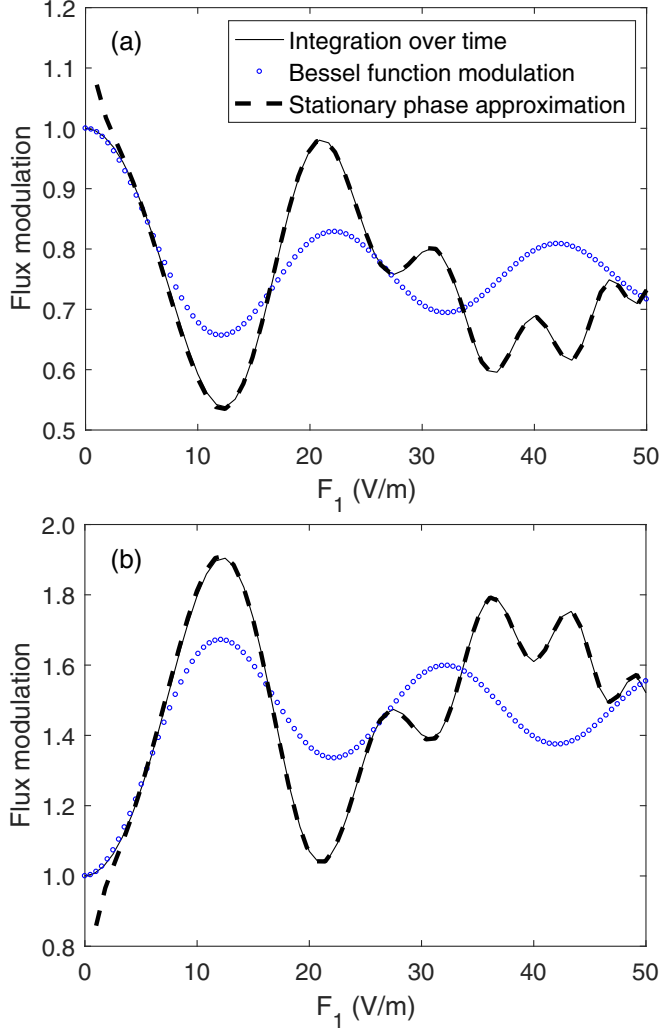
FIG. 9. Averaged image modulation at the detector center: the averaged temporal image over one period divided by the electron image in a static field only for (a) an *s*-wave source and (b) a *p*-wave source. The thin solid lines are calculated by direct integration over time. The open points result from using perturbation theory with a Bessel function [see Eq. (41)]. The bold dashed lines are obtained from stationary phase approximation in Eqs. (46) and (47).

A. Perturbation in the Bessel function

When the oscillating-field strength is weak enough, the electron dynamics is only weakly perturbed. The dominant change would come from the variation of the phase difference between the two trajectories reaching the detector simultaneously, since a small fractional change of the phase may cause an obvious modulation in the electron image. Therefore, it would be helpful to derive the formulas based on a perturbative expansion of $\Delta\tilde{S}$.

Following an action perturbation theorem in Ref. [42], the first-order expansion of $\Delta\tilde{S}$ in F_1 can be written as

$$\Delta\tilde{S} = \Delta S_0 - F_1|\Delta\tilde{Z}_s(\omega)|\sin(\omega t_f + \tilde{\beta}), \quad (37)$$

where $\tilde{\beta} = \arg[\Delta\tilde{Z}_s(\omega)]$,

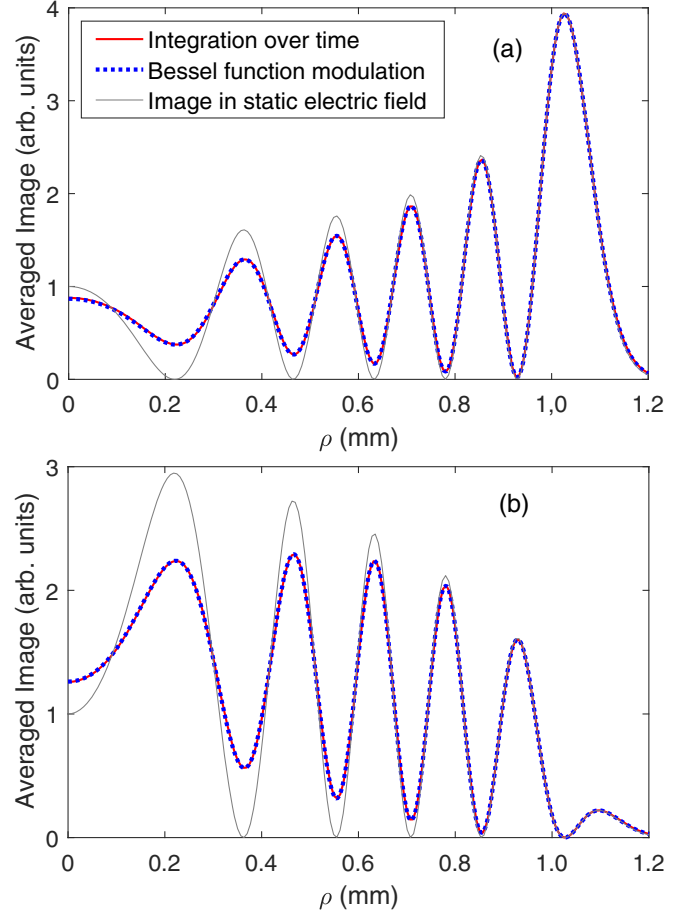$$\tilde{Z}_s(\omega) = \tilde{z}_s(\omega)T_s e^{-i\omega T_s} \quad (38)$$

FIG. 10. The averaged image in the perturbation regime with $F_1 = 5$V/m for (a) an *s*-wave source and (b) a *p*-wave source. The light thin solid lines are the electron flux in traditional PDM, shown here as a guidance for the weakening effect induced by the oscillating electric field. The calculation methods are indicated in the legend by the heavy red solid lines and the blue dotted lines.

is defined using the complex ac dipole moment $\tilde{z}_s(\omega)$ of the trajectory $z_s(\tau)$ in the static electric field, namely,

$$\tilde{z}_s(\omega) = \frac{1}{T_s}\int_0^{T_s} z_s(\tau)e^{i\omega\tau}d\tau, \quad (39)$$

and T_s is the time of flight of the electron in the static field. The integral in Eq. (39) is simple and the whole expression in Eq. (38) has the explicit form

$$\begin{aligned}
\tilde{Z}_s(\omega) = &-\frac{1}{2}F_0\left(\frac{2T_s}{\omega^2} - \frac{2}{\omega^3}\sin(\omega T_s)\right) \\
&+ k_0\cos(\theta_s)\left(\frac{1}{\omega^2} - \frac{1}{\omega^2}\cos(\omega T_s)\right) \\
&+ \frac{i}{2}F_0\left(\frac{T_s^2}{\omega} - \frac{2}{\omega^3} + \frac{2}{\omega^3}\cos(\omega T_s)\right) \\
&+ ik_0\cos(\theta_s)\left(-\frac{T_s}{\omega} + \frac{1}{\omega^2}\sin(\omega T_s)\right), \quad (40)
\end{aligned}$$

where θ_s represents the initially outgoing angle of the corresponding trajectory in the static electric field.
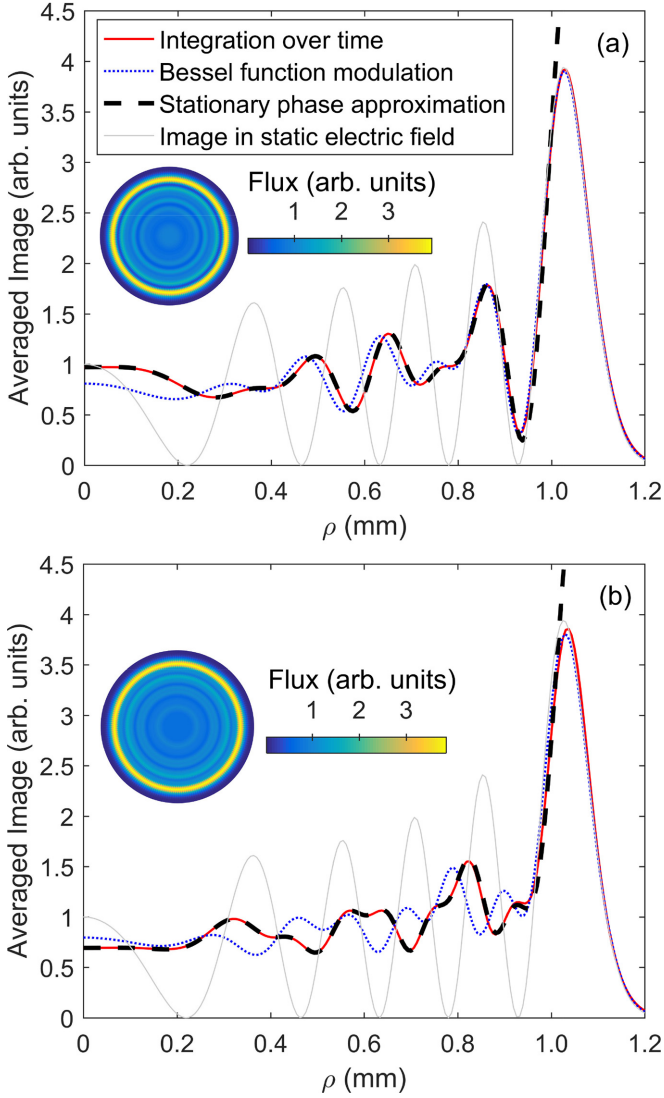
FIG. 11. Averaged image when the oscillating-field strength is increased: (a) $F_1 = 20$ V/m and (b) $F_1 = 40$ V/m, both for an s-wave source. The calculation methods are indicated in the legend by the different line styles. The pictures in each plot give the visual images one would see directly on the detector. The color bars suggest the relative intensity of the electron flux at each point.
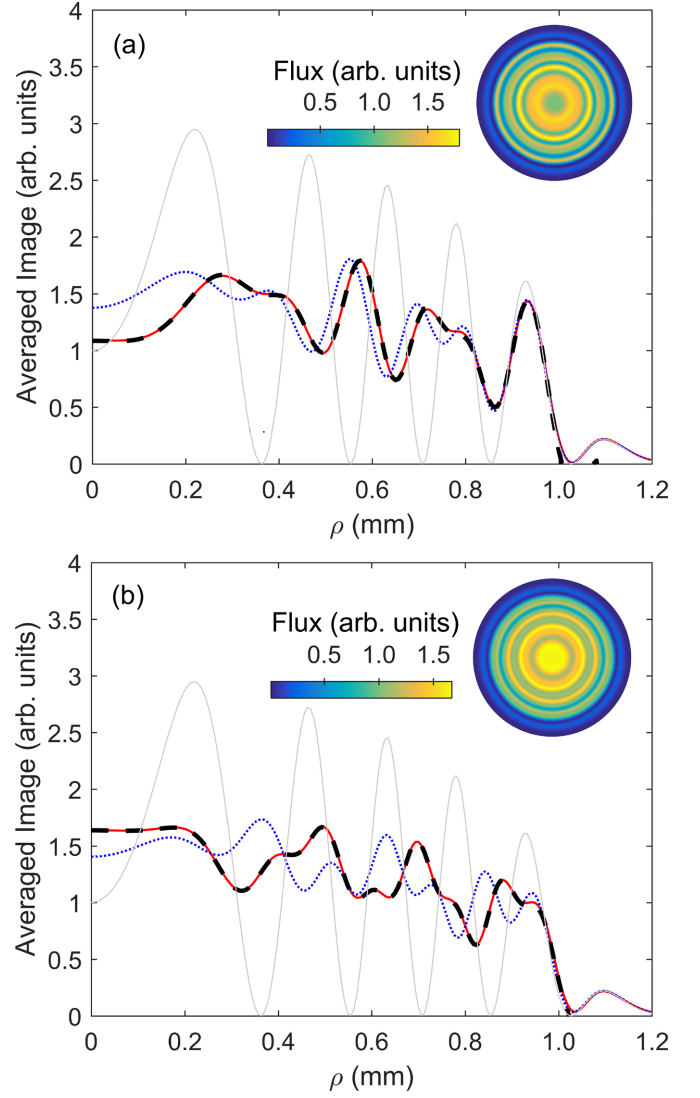

FIG. 12. Same as in Fig. 11 but for a p-wave source: (a) $F_1 = 20$ V/m and (b) $F_1 = 40$ V/m. The significance of lines is the same as in Fig. 11.

Using the standard form of integral connected with a Bessel function J_0 of the first kind,

$$\frac{1}{T}\int_0^T e^{-iF_1|\Delta\tilde{Z}_s(\omega)|\sin(\omega t_f + \tilde{\beta})} dt_f = J_0(F_1|\Delta\tilde{Z}_s(\omega)|),$$

the averaged result of $\cos(\Delta\varpi_{12})$ in Eqs. (24) and (25) can be expressed as

$$\frac{1}{T}\int_0^T \cos(\Delta\varpi_{12}) dt_f = J_0(F_1|\Delta\tilde{Z}_s(\omega)|)\cos\left(\Delta S_0 - \frac{\pi}{2}\right).$$

Therefore, the flux expression in Eq. (24) for an s-wave source can be approximated by

$$\overline{J_z} = -(p_{z_1}\tilde{A}_1^2 + p_{z_2}\tilde{A}_2^2)_{\text{static}} - [(p_{z_1} + p_{z_2})\tilde{A}_1\tilde{A}_2]_{\text{static}}$$
$$\times J_0(F_1|\Delta\tilde{Z}_s(\omega)|)\cos\left(\Delta S_0 - \frac{\pi}{2}\right) \quad (41)$$

in the perturbation region where the perturbation expansion of the phase difference is considered. The perturbed flux as in Eq. (41) for a p_z-wave source can also be obtained by inserting the Bessel function into the interference term in Eq. (25) and replacing all the other quantities by those corresponding values in a static electric field. To make it applicable near the classical boundary, the primitive form as in Eq. (41) should be repaired using Airy functions as in Eq. (29) by including the Bessel function in the prefactor and then extended into the classically forbidden region.

As shown in Eq. (41), the field-induced modulation of the averaged image is simply represented by the Bessel function when the applied oscillating field is weak enough in the perturbation region with respect to the static field. The calculations based on the perturbation formulas are displayed in Fig. 9 as a function of the oscillating-field strength. It can be observed that the averaged image with small values of F_1 in the perturbation region is described very well by the first-order perturbation theory in terms of the Bessel function. When
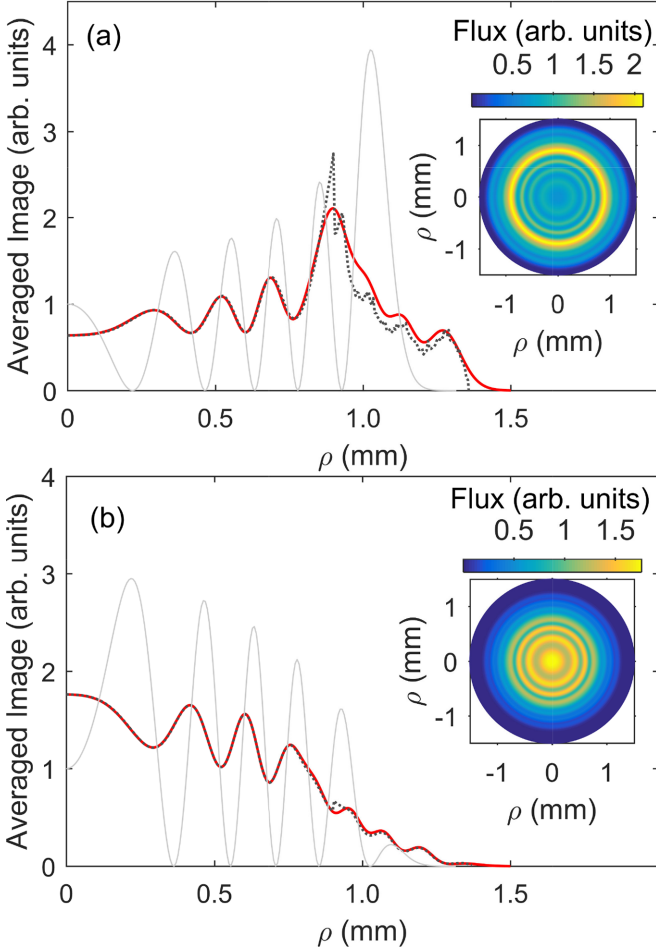
FIG. 13. Averaged image with $\omega/2\pi = 1$ MHz and $F_1 = 40$ V/m for (a) s-wave and (b) p-wave sources. The heavy red solid lines are calculated by integrating the temporal image in Figs. 6(a) and 6(b) after Eq. (36). The visual images on the detector are displayed in the insets, with the flux intensity at each point indicated by the color bar. The results from stationary phase approximations are shown by the dotted lines, where the classical static-field background in Eqs. (46) and (47) has been replaced by an averaged background over time using the time-dependent amplitude in Eq. (14). The light gray solid lines are the electron flux in traditional PDM.

$F_1 = 0$ V/m without an oscillating field applied, $J_0(0) = 1$ and Eq. (41) therefore represents the electron image in traditional PDM with only a static electric field [4,5,7].

Specific calculations for the averaged spatial image are also displayed in Fig. 10 for both s-wave and p_z-wave sources, where the applied oscillating-field strength ($F_1 = 5$ V/m) is 5% of the static field ($F_0 = 100$ V/m). The perturbation calculations with the Bessel function are in excellent agreement with the direct integration of the temporal image over time. Those observations can be fully understood now based on the perturbation formulas as in Eq. (41). The immediate observation in Fig. 10 is that the interference amplitude in traditional PDM is weakened by the added oscillating field, but the rainbows near the classical boundary are hardly affected. These observations can be understood very well by examining the behavior of the Bessel function. Note that the Bessel function

$J_0(x)$ is a monotonically decreasing function with x when x is small. By increasing the oscillating-field strength F_1 but still in the perturbation region, the Bessel function $J_0(F_1|\Delta\tilde{Z}_s(\omega)|)$ decreases monotonically and the oscillation amplitude of the electron image is weakened following Eq. (41). Near the classical boundary, the phase difference goes to zero gradually (Fig. 5) and the Bessel function $J_0(F_1|\Delta\tilde{Z}_s(\omega)|)$ therefore goes to a unity, which explains the relative stability of the averaged image near the classical boundary in Fig. 10.

B. Stationary phase approximation

Although the perturbation theory discussed above is quite successful in explaining the amplitude weakening effect and the monotonic behavior in the perturbation region, it fails to describe the oscillatory structure from the direct integration when the field strength becomes large. Hence, we proceed further to get a full understanding of the oscillatory behavior. Note that a large field strength causes a large variation of the phase difference $\Delta\tilde{S}$ over one period, resulting in many oscillations of the temporal image as in Fig. 3. For the averaged image as an integration of these oscillatory image, stationary phase approximation is a natural and important technique to grasp the dominant physics which is responsible for the main features in the averaged image.

Inspired by the stationary phase approximation, the dominant contribution to the integration of the temporal image is from the stationary phase points, namely, the extrema of $\Delta\tilde{S}$. Using the definition in Eq. (16), we have

$$\frac{\partial(\Delta\tilde{S})}{\partial t_f} = -\Delta E(t_f), \qquad (42)$$

where the partial derivative is taken by fixing the starting and ending positions of the trajectory. The stationary phase points correspond to $\Delta E(t_f) = E_1(t_f) - E_2(t_f) = 0$, suggesting that the two trajectories involved must have the same final energy when reaching the detector simultaneously. There is usually a limited number of pairs of trajectories satisfying this equal-energy condition. For our calculations in this work, we generally have two pairs of these trajectories over one period.

The averaged modulation part of the image can be readily expressed as

$$\frac{1}{T}\int_0^T (p_{z_1} + p_{z_2})\tilde{A}_1\tilde{A}_2 \cos\left(\Delta\tilde{S} - \frac{\pi}{2}\right)dt_f = \sum_{\text{SP}}\mathcal{M}_{\text{SP}} \quad (43)$$

for an s-wave source based on the stationary phase approximation, where the summation is over all those pairs of trajectories having the same final energy. For each stationary point,

$$\mathcal{M}_{\text{SP}} = \frac{\sqrt{2\pi}}{T\sqrt{\left|\frac{\partial[\Delta E(t_f)]}{\partial t_f}\right|}}[(p_{z_1} + p_{z_2})\tilde{A}_1\tilde{A}_2]_{\text{SP}}$$

$$\times \cos\left[\Delta\tilde{S}_{\text{SP}} - \frac{\pi}{2} - \frac{\pi}{4}\text{sgn}\left(\frac{\partial[\Delta E(t_f)]}{\partial t_f}\right)\right], \quad (44)$$

where the subscript SP indicates that the values of variables are calculated at the stationary phase point. The partial derivative

$$\frac{\partial[\Delta E(t_f)]}{\partial t_f} = \frac{\partial E_1(t_f)}{\partial t_f} - \frac{\partial E_2(t_f)}{\partial t_f}$$

should also be calculated at the stationary phase point, with

$$\frac{\partial E_i(t_f)}{\partial t_f} = -[F_0 + F_1 \sin(\omega t_f)]p_z(t_f) + \omega F_1 z_f \cos(\omega t_f)$$

$$- \frac{k_0[A(t_f) - A(t_i)]^2 \sin^2(\theta_i)}{(t - t_i)[k_0 - F(t_i)(t - t_i)\cos(\theta_i)]}$$

$$+ \frac{2E_k(t_f)F(t_i)\cos(\theta_i)}{k_0 - F(t_i)(t - t_i)\cos(\theta_i)}, \tag{45}$$

where $E_k(t_f)$ is the final kinetic energy when reaching the detector.

The background part of the image, like the term $-p_{z_1}\tilde{A}_1^2 - p_{z_2}\tilde{A}_2^2$ in Eq. (24), corresponds to the classical distribution without the quantum-interference oscillations. With the oscillating field applied, the original electron distribution in a static field would be redistributed as indicated by the arrival-time plot in Fig. 2 and the accumulated amplitudes in Fig. 7(b). However, when this new distribution is integrated over one period, the averaged distribution is expected to have little difference from the averaged background in a static field. Therefore, for a satisfied approximation, one can simply take the image background in a static field as the averaged background of the image with an oscillating field.

Finally, we arrive at the simple expression

$$\overline{J_z} = -\left(p_{z_1}\tilde{A}_1^2 + p_{z_2}\tilde{A}_2^2\right)_{\text{static}} - \sum_{\text{SP}} \mathcal{M}_{\text{SP}} \tag{46}$$

for an s-wave source and

$$\overline{J_z} = -\left[p_{z_1}\tilde{A}_1^2 \cos^2(\theta_{i1}) + p_{z_2}\tilde{A}_2^2 \cos^2(\theta_{i2})\right]_{\text{static}}$$

$$- \sum_{\text{SP}} \mathcal{M}_{\text{SP}}[\cos(\theta_{i1})\cos(\theta_{i2})]_{\text{SP}} \tag{47}$$

for a p_z-wave source. After Eqs. (46) and (47), the accumulated image over time contains a background plus a summation of oscillatory terms and each oscillatory term corresponds to a pair of two trajectories arriving at the same point simultaneously with the same final energy.

Specific calculations using Eqs. (46) and (47) are shown in Figs. 9, 11, and 12. One may notice that the semiclassical calculations fails in two regions. When F_1 goes to zero in Fig. 9, the formulas in Eqs. (46) and (47) fail because $\partial[\Delta E(t_f)]/\partial t_f$ goes to zero. Near the classical boundary in Figs. 11 and 12, the semiclassical results diverge because the amplitudes $\tilde{A}_1$ and $\tilde{A}_2$ go to infinity at the caustic. By comparing the averaged images obtained in Figs. 11 and 12, it can be found that a p_z-wave source as in Fig. 12 might be a superior choice to observe the averaged electron image in an experiment. This is because the node structure in the initially p_z-wave angular distribution makes most of the electrons naturally avoid the classical boundary on the detector. Most of the electrons therefore arrive at the inner region where the averaged image is to be studied.

Except for those intrinsic defects of the semiclassical approximation, excellent agreement is achieved almost everywhere in Figs. 9, 11, and 12 by comparing with the direct integration of the temporal image over time. This confirms the physical picture established above from the stationary phase approximation: The field-induced averaged modulation is dominantly contributed by the quantum interferences between each pair of trajectories arriving at the same spatial-temporal point with the same final energy. This semiclassical picture provides a simple and intuitive understanding for those modulations left in the averaged image, which represents a generalized version of the semiclassical picture established for traditional PDM in the early days [4].

Those rainbow structures near the image edge also exhibit distinctive features. The flux intensity near the image edge in Figs. 11 and 12 is almost the same as that in traditional PDM. This is readily understood following the same argument for the vanishing of temporal interferences near the classical boundary based on Fig. 5. It is also related to the stability of those locations of the temporal image edge. However, the situation will be different if the image edge is distorted obviously as in Fig. 6. The averaged image corresponding to Fig. 6 is shown in Fig. 13. The temporal images in Figs. 6(a) and 6(b) are integrated after Eq. (36), given by the heavy red solid curves in Figs. 13(a) and 13(b). The main difference of the image in Fig. 13 from those in Figs. 11 and 12 is that the sharp image edge as in traditional PDM is broadened on average, corresponding to the large-range distortion of the classical boundary in Fig. 6.

The semiclassical interference picture established above is actually general, also applicable for the case in Fig. 13. The rest of the interferences observed in Fig. 13 are also contributed by those pairs of trajectories reaching the detector simultaneously with the same final energy, which are quantitatively given by those terms of summation in Eqs. (46) and (47). Note that the static-field approximation used for the classical background in Eqs. (46) and (47) is now invalid; one should replace it as a direct integration over time using the time-dependent amplitude in Eq. (14). The corresponding calculations are shown by the dotted lines in Fig. 13, which agree well with those heavy solid lines. The imperfect background of the dotted lines for the broadened edge is caused by the divergence of the semiclassical amplitude at each classical caustic, while for a p-wave source this divergence is largely suppressed by the term $\cos\theta_i$, with $\theta_i \approx \pi/2$, at the caustic [see Eq. (25)] when the detector is far away from the electron source.

V. CONCLUSION

We have systematically explored the field-induced modulations of the electron image in traditional PDM when a weak oscillating electric field is applied. Compared to previous studies with only a static field [1,4–7] or a pure oscillating field [33,39,40], the present system provides periodic modulation in time and bunching effects in PDM. Both the temporal and the accumulated images have been examined in detail. All of the phenomena and related features can be understood based on the established physical pictures. The present work represents an effort to generalize the concept of spatial interferences in traditional PDM to temporal-spatial interferometry from a theoretical perspective. It represents a step towards future studies on quantum imaging spectrometry, especially for generalizing traditional PDM by including the temporal effects. Similar ideas can be extended to study photoionization microscopy.

Once the oscillating field is applied, the photoelectron dynamics oscillates with the field periodically, and the photoelectron image is therefore modulated in both the temporal and spatial dimensions. The variation of the spatial image with time depends on specific locations on the detector. The electron flux near the image center can be easily modulated. The photoelectron rainbow structure near the image edge is almost unchanged as long as the oscillating-field period is much smaller than the time of flight for the electron reaching the detector or the oscillating field is weak enough. If the added oscillating field is sufficiently strong and its period is also large enough that the electron could reach the detector within a fraction of the period, the photoelectron rainbow structure is distorted with time obviously owing to a large-range variation of the classical boundary.

The interference oscillations are generally enriched by increasing the oscillating-field strength. The electron tends to be clustering in the time domain, where the number of oscillations increases gradually. When the oscillating-field strength is comparable to the static-field value, an electron bunching effect has been observed. Many electrons from a large range of initial time instants arrive at the detector in a very narrow window of time, resulting in a locally high electron intensity on the detector. The electron flux forms a train of intense coherent pulses impacting on the detector. Depending on different electron sources, one can observe a periodic flash of an extremely bright ring near the image edge or bright oscillations near the image center. The combination of the static and the oscillating electric fields is essential for these temporal phenomena.

The averaged image over one period has been investigated, corresponding to the accumulated image in an experiment over many cycles of the oscillating field. We find that the locations of those interference rings in traditional PDM are stable if the oscillating field is weak enough, but their oscillation amplitudes are weakened. It can be approximately described by a Bessel function in the perturbation regime. This pure weakening effect also indicates the stability of traditional PDM in measuring the electron affinities against any weak noises of an oscillating field, because the number of interference rings remains unchanged. By increasing the field strength, some typical oscillations are formed and left in the averaged electron image. A semiclassical picture is established based on stationary phase approximations. It turns out that the oscillations are contributed by the quantum interferences between electron waves propagated along different

classical trajectories which arrive at the same point on the detector simultaneously with the same final energy.

Ultimately, a practical question is how difficult it is to observe the temporal phenomena in a real experiment. From our theoretical perspectives, the applied field frequency should be much smaller than the laser frequency for detaching the electron. An upper limit of the field period T is also restricted by the time of flight τ for the electron reaching the detector. The time-dependent measurement is meaningless if $T \gg \tau$ where the total field strength is approximately static for each electron flying to the detector. The value of τ in traditional PDM with the parameters we used is about 0.24 μs. Therefore, the field period can be tuned in a range from picoseconds to microseconds for a meaningful temporal experiment.

The main challenge would be related to the temporal resolution required for collecting the time-dependent images. The oscillating-field frequencies of 100 and 1 MHz we used for demonstration correspond to field periods of 10 ns and 1 μs, respectively. A resolution around 1 ns is sufficient to observe most of those time-dependent features in the electron image. We note that the up-to-date detector with microchannel plates has been pushing the temporal resolution to tens of picoseconds [43–46]. This resolution is already high enough to detect the effects discussed in the present work. Once those temporal phenomena could be realized in experiments, many possibilities may be opened from a time-dependent viewpoint.

It is helpful to briefly recall the long history of developments of traditional PDM. It took decades to go from the early theoretical discussions of the quantum interferences [4–6] to the experimental observations [1–3] and applications for extracting accurate electron affinities of atoms [8]. The key element is the quantum interferences of a photoelectron induced by external fields. In the present work we explored the spatiotemporal dynamics of the electron pulses manipulated by an additional external oscillating field, revealing the time modulation and bunching effect as shown in the images. Our theoretical study may also inspire various applications in the future.

[1] C. Blondel, C. Delsart, and F. Dulieu, Phys. Rev. Lett. **77**, 3755 (1996).

[2] C. Blondel, C. Delsart, F. Dulieu, and C. Valli, Eur. Phys. J. D **5**, 207 (1999).

[3] C. Delsart, F. Goldfarb, and C. Blondel, Phys. Rev. Lett. **89**, 183002 (2002).

[4] M. L. Du, Phys. Rev. A **40**, 4983 (1989).

[5] I. I. Fabrikant, Sov. Phys. JETP **52**, 1045 (1980).

[6] Y. N. Demkov, V. D. Kondratovich, and V. N. Ostrovskii, JETP Lett. **34**, 403 (1981).

[7] C. Bracher, T. Kramer, and M. Kleber, Phys. Rev. A **67**, 043601 (2003).

[8] C. Valli, C. Blondel, and C. Delsart, Phys. Rev. A **59**, 3809 (1999).

[9] C. Blondel, W. Chaibi, C. Delsart, C. Drag, F. Goldfarb, and S. Kröger, Eur. Phys. J. D **33**, 335 (2005).

[10] R. J. Peláez, C. Blondel, M. Vandevraye, C. Drag, and C. Delsart, J. Phys. B **44**, 195009 (2011).

[11] D. Bresteau, C. Drag, and C. Blondel, Phys. Rev. A **93**, 013414 (2016).

[12] D. Bresteau, C. Drag, and C. Blondel, J. Phys. B **52**, 065001 (2019).

[13] C. Ning and Y. Lu, J. Phys. Chem. Ref. Data **51**, 021502 (2022)

[14] C. Bracher and J. B. Delos, Phys. Rev. Lett. **96**, 100404 (2006).

[15] C. Bracher, T. Kramer, and J. B. Delos, Phys. Rev. A **73**, 062114 (2006).

[16] S. Gao, G. C. Yang, S. L. Lin, and M. L. Du, Eur. Phys. J. D **42**, 189 (2007).

[17] C. Bracher and A. Gonzalez, Phys. Rev. A **86**, 022715 (2012).

[18] B. C. Yang, J. B. Delos, and M. L. Du, Phys. Rev. A **88**, 023409 (2013).

[19] W. Chaibi, C. Blondel, C. Delsart, and C. Drag, Europhys. Lett. **82**, 20005 (2008).

[20] W. Chaibi, R. J. Peláez, C. Blondel, C. Drag, and C. Delsart, Eur. Phys. J. D **58**, 29 (2010).

[21] X. J. Chen, K. Titimbo, and M. L. Du, Europhys. Lett. **123**, 30008 (2018).

[22] K. Titimbo, X. J. Chen, and M. L. Du, Phys. Rev. A **100**, 013418 (2019).

[23] C. Nicole, H. L. Offerhaus, M. J. J. Vrakking, F. Lépine, and C. Bordas, Phys. Rev. Lett. **88**, 133001 (2002).

[24] F. Lépine, C. Bordas, C. Nicole, and M. J. J. Vrakking, Phys. Rev. A **70**, 033417 (2004).

[25] L. B. Zhao and J. B. Delos, Phys. Rev. A **81**, 053417 (2010).

[26] L. B. Zhao and J. B. Delos, Phys. Rev. A **81**, 053418 (2010).

[27] L. Wang, H. F. Yang, X. J. Liu, H. P. Liu, M. S. Zhan, and J. B. Delos, Phys. Rev. A **82**, 022514 (2010).

[28] S. Cohen, M. M. Harb, A. Ollagnier, F. Robicheaux, M. J. J. Vrakking, T. Barillot, F. Lépine, and C. Bordas, Phys. Rev. Lett. **110**, 183001 (2013).

[29] A. S. Stodolna, A. Rouzée, F. Lépine, S. Cohen, F. Robicheaux, A. Gijsbertsen, J. H. Jungmann, C. Bordas, and M. J. J. Vrakking, Phys. Rev. Lett. **110**, 213001 (2013).

[30] A. S. Stodolna, F. Lépine, T. Bergeman, F. Robicheaux, A. Gijsbertsen, J. H. Jungmann, C. Bordas, and M. J. J. Vrakking, Phys. Rev. Lett. **113**, 103002 (2014).

[31] P. Giannakeas, F. Robicheaux, and Chris H. Greene, Phys. Rev. A **91**, 043424 (2015).

[32] M. Deng, W. Gao, Rong Lu, J. B. Delos, L. You, and H. P. Liu, Phys. Rev. A **93**, 063411 (2016).

[33] B. C. Yang and F. Robicheaux, Phys. Rev. A **92**, 063410 (2015).

[34] S. Fleischer, Y. Zhou, R. W. Field, and K. A. Nelson, Phys. Rev. Lett. **107**, 163603 (2011).

[35] K. N. Egodapitiya, S. Li, and R. R. Jones, Phys. Rev. Lett. **112**, 103002 (2014).

[36] S. Li and R. R. Jones, Phys. Rev. Lett. **112**, 143006 (2014).

[37] B. C. Yang and F. Robicheaux, Phys. Rev. A **90**, 063413 (2014).

[38] B. C. Yang and F. Robicheaux, Phys. Rev. A **91**, 043407 (2015).

[39] H. Ambalampitiya and I. I. Fabrikant, Phys. Rev. A **95**, 053414 (2017).

[40] S. U. Khan, X. J. Chen, S. Wang, W. C. Jiang, and P. Yan, J. Electron. Spectrosc. Relat. Phenom. **256**, 147143 (2022).

[41] E. P. Wigner, Phys. Rev. **73**, 1002 (1948).

[42] M. R. Haggerty and J. B. Delos, Phys. Rev. A **61**, 053406 (2000).

[43] D. A. Debrah, G. A. Stewart, G. Basnayake, A. Nomerotski, P. Svihra, S. K. Lee, and W. Li, Rev. Sci. Instrum. **91**, 023316 (2020).

[44] G. Basnayake, Y. Ranathunga, S. K. Lee, and W. Li, J. Phys. B **55**, 023001 (2022).

[45] E. Orunesajo, G. Basnayake, Y. Ranathunga, G. Stewart, D. Heathcote, C. Vallance, S. K. Lee, and W. Li, J. Phys. Chem. A **125**, 5220 (2021).

[46] A. S. Tremsin, J. V. Vallerga, and O. H. W. Siegmund, Nucl. Instrum. Methods Phys. Res. Sect. A **949**, 162768 (2020).